Spectral Observations of Micro Quasar GRO J1655-40 in 2005 Outburst

Ytsen K. Haringa
Supervisor: Mariano Mendez

July 7, 2009

Abstract

We present a spectral analysis of black hole X-ray transient GRO J1655-40 during its 2005 outburst using the data from RXTE (PCA & HEXTE) and XMM-Newton (EPIC-PN). RXTE provided full coverage at low spectral resolution whereas XMM-Newton provided six high spectral resolution spectra. The fits of the RXTE spectra enabled us to chart the behavior of several parameters during the whole outburst. The XMM-Newton spectra revealed several absorption features attributed to FeXXV, FeXXVI and NiXXVIII. The optical depth of these absorption features were used to give us some insight into the geometry of the ionized region surrounding the source. The source followed the canonical picture of outburst phases for the majority of the outburst, however for the first time a super soft anomalous phase was discovered which deviated from this picture. Also an extreme point was observed during the peak of the outburst. This was the first time such an extreme point was observed in this source and only the second time in half a dozen X-ray transients. We also confirm some relationships between properties of the accretion disk and the power-law feature. The XMM-Newton data revealed an ionized region with geometry parameters in the same order as similar sources.

1 Introduction

GRO J1655-40 is a very interesting and extensively observed transient black hole X-ray binary. It was discovered in 1994 (Zhang et al. 1994) using the Burst and Transient Source Experiment (BATSE) on board the Compton Gamma Ray Observatory. Because it is so well observed the data collected is quite numerous and precise. This binary system appears to be at a distance of 3.2 ± 0.2 kpc and consists of a 7.0 ± 0.2 $M_\odot$ black hole orbiting a 2.3 $M_\odot$ F3 IV - F6 IV companion star in a 2.6 day orbit (Orosz & Bailyn 1997). Previous observations of this source during outburst (Sobczak et al. 1999) indicate that the accretion disk inner radius reaches well inside the innermost stable orbit of a non-rotating black hole, which suggests that the black hole is rapidly rotating. Observations of this system in the radio band indicate jets which appear to be superluminal; this puts GRO J1655-40 in the microquasar category (Smith et al. 1997). The jet is likely to be viewed at $69.5^\circ \pm 0.1^\circ$, although the inner disk inclination can be as high as 85° (Orosz & Bailyn 1997, Hjellming & Rupen 1995) which suggests a misalignment between the inner-disk and the rest of the binary system (Lense-Thirring effect). The inclination of the disk is measured under the assumption that the observed radio jet is aligned perpendicular to the accretion disk.

We are able to detect this system in X-rays because the vicinity of the secondary star to the black hole produces a very energetic interaction between the two companions. The strong gravitational force from the black hole funnels a stream of gas extracted from the surface of the star onto an accretion disk orbiting the black hole. Via this accretion disk the gas is fed onto the black hole and in the process some of the gravitational potential energy is converted into high energy photons (X-ray) which are detectable by orbiting instruments like XMM-Newton, Chandra and RXTE (Rossi X-ray Timing Explorer).

The fact that GRO J1655-40 is a transient means that this system regularly experiences an "outburst"; this is characterized by a dramatic increase of X-ray flux over a period of several months. There have been three documented outbursts of GRO J1655-40 so far. The discovery of GRO J1655-40 in 1994 was due to its first recorded outburst; this was picked up by the BATSE instrument. Subsequent outbursts were observed in 1996/1997 (Sobczak et al. 1999) and 2005 with RXTE. The 2005 outburst is the subject of my master thesis. The exact nature of these outbursts is still a matter of discussion, although it is logical to assume a relation between the matter input from the secondary star onto the accretion disk and the radiation output from the disk.

One of the goals of this research is to use the high spectral-resolution XMM-Newton data to see if there is a development in the ratio of several highly ionized iron lines, which were observed during the progression of the outburst. This ratio can be used to gain some insight into the geometry of the ionized region surrounding the source. The RXTE data have a lower spectral-resolution than the XMM-Newton data, but they are much more numerous with daily observations. These data span the whole outburst, so they are very useful in getting a clearer picture of the development of certain observables during the different phases of this outburst. The combination of these two datasets will help in the understanding of the mechanisms driving the outburst by offering complementary information during specific parts of this event.

This report is presented in the following way. In section 2 We give some background information about the properties and processes which are important for this source. Section 3 contains a description of the telescopes and instruments. Section 4 treats the observations used and the data analysis of these observations. In section 5 the results are presented. The discussion of these results is treated in section 6.

2 Background

This section contains some background information about objects and processes described in this report.

2.1 X-ray Binaries

Research starting as early as the 19th century has shown that many stars are part of a binary or multiple star system. One class of these systems are the X-ray binaries, which as the name suggests are luminous in X-rays. These systems consist of a normal optically visible star and a compact companion, which can be a white dwarf, neutron star or black hole. X-ray binaries are divided into two subclasses according to the mass of the optically visible star: Low-Mass X-ray Binary (LMXB) and High-Mass X-ray Binary (HMXB). Some of these systems have been designated as micro-quasar; these are identified by a pair of radio-jets emanating from the center of an accretion disk around the black hole or neutron star. The name is derived from the much larger active galactic nuclei because of the similarities in the morphology of the objects.
Because of the fact that GRO J1655-40 is an LMXB and is identified as being a micro-quasar, I shall describe the structure of this object more extensively. As mentioned before, the system consists of an optically visible star and a compact object luminous in X-ray, let us take a black hole as compact object as it is the likely scenario in the case of GRO J1655-40. In the case of an LMXB like GRO J1655-40, the strong gravitational force exerted on the star by the black hole causes material from the star filling up the Roche lobe. The material in the Roche lobe passes through the Lagrangian point (L1) and ends up in a accretion disk around the black hole. The material falling into the black hole gets heated up, and gravitational potential energy is converted into radiation. These photons strip the atoms and ions in the inner part of the accretion disk from most of their electrons. Part of these free electrons gets disconnected from the disk through photon pressure or interaction with the magnetic field; these free electrons can end up in a corona which surrounds the source. These electrons scatter part of the photons originating from the central source and either decrease (Compton effect) or increase (inverse-Compton effect) the energy of those photons. The changes in photon energy through these effects show up as a change in photon distribution along the energy axis in the spectrum. Furthermore, photons can be scattered back towards the accretion disk and re-emitted

into space, which can produce emission or absorption features in the spectra. The nature and origin of the electron clouds scattering the photons is still a matter of debate. These clouds could be gravitationally connected to the source (corona) or part of a thermal wind or jet blowing particles into the surrounding medium (Miller et al. 2008). As said before, GRO J1655-40 was observed to have radio jets and the X-rays from near the central source can heat up the gas in the accretion disk through the Compton effect until they reach escape velocity, this can be the engine behind thermal winds in accreting systems (Miller et al. 2008). Therefore it is likely to assume that these scattering regions are the sum of several features.

Observations of GRO J1655-40 have indicated the presence of superluminal jets (Hjellming & Rupen 1995; Tingay et al. 1995). The most widely accepted theory about the formation of these jets is that the magnetic field around the accretion disk gets dragged by the spin of the black hole. The magnetic field gets tangled up in the accretion disk tightening the field lines and forcing up relativistic material forming the jets. The magnetic field produced by the accretion disk is not strong enough to be the sole engine behind these jets, it is therefore thought that this tangled magnetic field mearly acts as a collimator for the jet rather then the energy source (Fendt 2006). The power behind the ejection of material via this jet seems to be caused by internal shocks (Fender, Homan & Belloni 2009). From Figure 1 we see that radio emission is detected in the low/hard state at the beginning and the end of the outburst (see next section for a description of states). These radio detections are observed to have a flat spectrum, which appears to indicate a steady and continuous ejection (wind?)(Fender, Homan & Belloni 2009). In the hard/soft transition a radio flare is observed (Rupen, Dhawan & Mioduszewski 2005). This flare has a steep spectrum which can be linked to the ejection of a blob of material radiating in radio (jet?).

2.2 Outburst Phases

The energy output of a X-ray binary system is observed to remain stable at a very low level (sometimes undetectable) for long periods of time. This quiescent mode is sometimes interrupted by a period of massive increase in flux. This so-called "Outburst" often lasts for several months and repeats itself after a couple of years. The nature of these outbursts is still a matter of debate. There is a consensus that the increase in X-ray flux must be the result of an increase in matter inflow ($F_x \propto \dot{M}$), but the mechanism(s) behind this matter flow increase is (are) still largely unknown.

The outburst experienced by this and several other sources is not a steady process. These outbursts go through a number of phases and the understanding of the physical background behind these phases may shed some light on the conditions of the binary system. The development of the out-

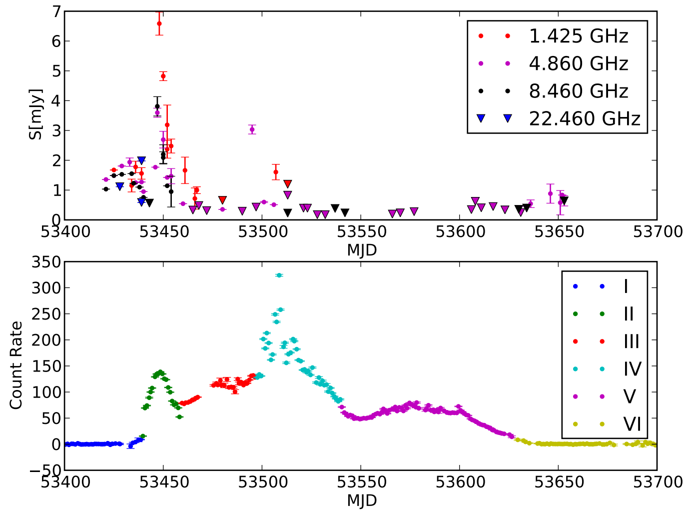

Figure 1: **Top**: the radio emission of GRO J1655-40 during outburst. **Bottom**: the ASM lightcurve of the outburst.

burst can be followed by examining the hardness of the spectrum. The hardness indicates the ratio between the hard X-ray photons (e.g. 6.0 - 200.0 keV) and the soft X-ray photons (e.g. 3.0 - 6.0 keV). If the spectrum is dominated by photons with low energy, the source is said to be in the soft state. If the opposite is true, the source is designated as being in the hard state. Another variable to consider is the amount of flux received, low, intermediate or high. So if the spectral state is low-hard, then the amount of photons received is low and they are mostly in the high energy part of the spectrum. This classification includes five spectral states: quiescent state, low-hard state (LHS), intermediate (hard or soft) state ((H)(S)IS), high-soft (thermally dominant) state (HSS) and very high (powerlaw dominant) state (McClintock & Remillard 2006).

The canonical model of an outburst is described in the following way. As said before, the source spends most of its time in the quiescent state where it can not be detected by XMM-Newton or RXTE. When the source goes into outburst it starts out in the low/hard state. In this state the accretion disk is still quite weak and the inner radius of the disk lies far away from the compact object which is surrounded by a corona of charged particles. The spectrum is dominated by a high-energy power-law feature with a photon index (Γ) of about 1.5; this power law is produced by up-scattered soft photons which originate from a cool disk. Sources in this state often show emission in radio, which indicates the presence of a radio jet or wind.

After the low/hard state the source enters the intermediate state. This state is situated in the transition between the hard and the soft state and it usually lasts only a couple of days. After this rapid transition from the hard state to the soft state a new phase of the outburst is reached, the high/soft state. Not only is there an increase in the number of soft photons, but the total photon count rises to several order of magnitude above the low/hard state. The transition to the soft state coincides with a decrease of the accretion disk inner radius. Consequently the disk is increasing in temperature and the number of soft disk photons are becoming much more numerous. The increase of soft photons results in a softer spectrum and the cooling of the surrounding corona through Compton scattering. As a result of these developments, the disk blackbody becomes the more dominant feature in the spectrum and the power law becomes steeper ($\Gamma \sim$ 2-3).
The peak(s) of an outburst is (are) represented by the very high state. As the name suggests, this state exhibits a very high photon count. This phase has a hard spectrum and is therefore dominated by a power-law feature.
These are the "standard" outburst states, but some sources, including GRO J1655-40, show some anomalous states which do not fit in the canonical model. We will discuss this in a later section.

3 Instruments

In this section I will describe the telescopes and instruments used to obtain the data for this research.

3.1 XMM-Newton

The XMM-Newton satellite (X-ray Multi-Mirror Mission Newton) was launched in December 1999 in a very eccentric elliptical orbit (apogee 114.000 km, perigee 7.000 km). This satellite contains three X-ray telescopes with a combined collecting area of 4.300 cm^2. Two of these three telescopes have EPIC (European Photon Imaging Cameras) in the focal plane with MOS (Metal Oxide Semi-conductor) CCD arrays. These CCD's are placed behind the telescopes which are equipped with the gratings of the RGS (Reflection Grating Spectrometers), these reflect about 44% of the incoming flux onto the MOS cameras. The third telescope has a unobstructed beam which focusses on the EPIC-PN CCD's; this is the instrument I use for my research. The unobstructed view of the PN instrument gives it a larger effective area than the MOS instruments; the EPIC-PN is also more sensitive in the higher energy range (E $>$ 10.0 keV). These are the main reasons for using this instrument. The field of view of these EPIC cameras encompasses about 30 arcmin in the energy range 0.15 - 15.0 keV. The instruments have a moderate spectral ($\frac{E}{\delta E} \sim$ 20-50) and angular (PSF, 6 arcsec FWHM) resolution.

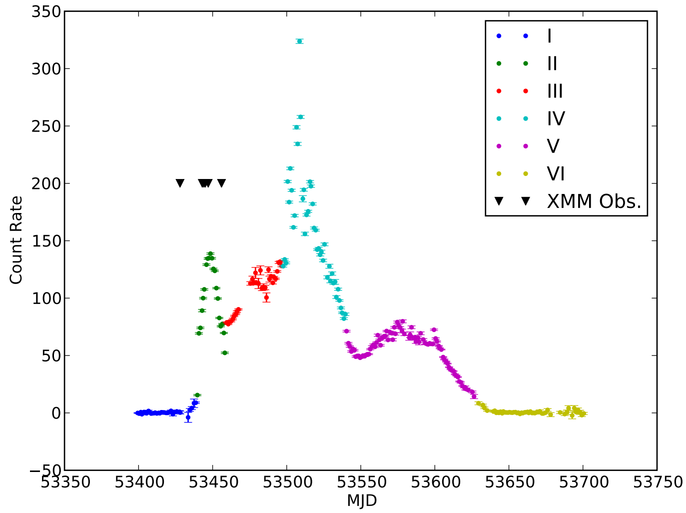

Figure 2: The ASM lightcurve of the 2005 outburst of GRO J1655-40. The black triangles point to the positions of the XMM-Newton observations.

During the 2005 outburst of GRO J1655-40, the XMM-Newton satellite observed the source six times within a timeframe of about one month. These observations covered the beginning of the outburst as was made clear by the lightcurve of the source obtained with the All Sky Monitor (ASM) instrument (2.0 - 12.0 keV) on-board the RXTE satellite (between MJD 53428 and 53456 in Figure 2).

3.2 RXTE

In order to get a more complete picture of the outburst of GRO J1655-40, we used data obtained from instruments aboard the RXTE (Rossi X-ray Timing Explorer). During the outburst about 450 pointed observations were made of which 101 were used for this project. The RXTE was launched on 30 December 1995 from Cape Canaveral. This satellite has three instruments on board, the Proportional Counter Array (PCA), to cover the lower part of the energy range (3.5 - 20.0 keV), the HEXTE (High Energy X-ray Timing Experiment), for the upper energy range (15.0 - 200.0 keV) and the ASM (All Sky Monitor), which scans about 80% of the sky every orbit at timescales of 90 minutes or longer in the 1.5 to 12.0 keV band.
The PCA is divided into five individual proportional counter units (PCU's); we only used the PCU2 instrument as opposed to all five of the PCU instruments (PCU0 - PCU4), because this was the only one that worked during

the whole duration of the outburst. The HEXTE instrument consists of two clusters (A & B) which alternatively are pointed at the observed source and the background to get a background subtracted observation. At the moment of the outburst cluster A was stuck in the background mode, so cluster B was used to observe both the source and the background.

4 Observation and Data Reduction

This is the description of the analyses of 6 (moderate spectral resolution) XMM-Newton and 101 (low spectral resolution) RXTE observations of the micro quasar GRO J1655-40 during its 2005 outburst. The outburst started on March 10 2005, and ended at the beginning of October of the same year, thus lasting about 200 days. X-ray spectra were obtained using the EPIC-PN instrument aboard the XMM-Newton and the PCA and HEXTE instruments aboard the RXTE. The EPIC-PN instrument covers the X-ray band between 0.5 and 12.0 keV. The PCA covers the X-ray spectrum in the band 3.5 - 20.0 keV, whereas the HEXTE covers the band 15.0 - 200.0 keV.

4.1 XMM-Newton

We reduced the XMM-Newton Observation Data Files (ODF) using the program SAS (Science Analysis Software, version 8.0.0) with the appropriate calibration files. We extracted event files from the ODF for the EPIC-PN, EPIC-MOS and RGS instruments, using the SAS commands **epproc**, **emproc** and **rgsproc** respectively. The observations of the source with the EPIC-PN were done in timing mode, which enables very high time resolution. Only the central CCD (CCD0) is used and the data from the area of this CCD is collapsed into one column generating a 100×1 pixel image. This is read out by the instrument every 1.5 ms. The following actions were applied to the data obtained with the EPIC-PN instrument: Using the SAS program **xmmselect**, the lightcurve was examined in order to exclude background flares caused by the Sun. The same program was used to produce a spectrum of the source and the background for each of the six observations, the parameters used for this process are given in table 4.1. The response and ancillary files were created with **rmfgen** and **arfgen** respectively (see section 4.4 for a description of these files and the procedures).
An important thing to consider with a bright source is pile-up. Pile-up occurs when two or more X-ray photons deposit charge in a single CCD pixel, or in neighboring pixels, within one read-out cycle, which would produce a deformed spectrum. With pile-up, the instrument would interpret several photons with relatively low energy as one photon with high energy, therefore the flux goes down and the source is dominated by high-energy photons. No

pile-up was detected in this observation. Using the program **pharbn**, a re-binned version of these spectra were produced. The re-binning was done to sample the spectra at a minimum of three channels per resolution element. The re-binned spectrum has a minimum of 70 counts per channel; this count rate is high enough for the distribution of counts to resemble a Gaussian distribution, which is required to be able to use χ^2 to find the best-fit models. The spectra were fitted with appropriate models using XSPEC (Xray Spectral Fitting Package, version 11.3.2, Arnaud 1996). The components used in this analyses to fit the spectra are briefly mentioned here and described in more detail in section 4.3. All the models of the six spectra have some base components in common. First the component **phabs** represents the absorption of the ISM. The component **diskbb** is the contribution of a multi-color blackbody spectrum due to a geometrically thin, optically thick accretion disk (Shakura & Sunyaev, 1973). Because the accretion disk has a temperature gradient in the radial direction, the **diskbb** is a sum of blackbodies at different temperatures. **powerlaw** represents a power-law component, due to non-thermal emission. The strength of these components, especially the last two, can vary significantly between the six spectra. There are two Gaussian components that also appear in each spectra. These emission/absorption lines represent elements present in the instruments; the CCD detectors contribute a Si line at 1.844 keV and the telescope mirror gives a Au line at 2.25 keV. Two recurring features in the spectra are interpretted as the Fe XXV (6.70 keV) and Fe XXVI (6.97 keV) absorption lines which are present in the last five spectra (see figure 3). Another feature was found in three of the spectra at 8.08 keV, this was identified as a NiXXVIII absorption line. A **laor** profile was fitted in two of the spectra, this feature can appear when a line is broadened by a relativistically rotating disk. The broadening is due to gravitational redshift, Doppler shift and boosting. An **edge** component was added, representing the effect of bound-free transitions when a photon with an energy just above the energy of the K-shell electron interacts with the ion. In the case of Fe XXV and Fe XXVI the edge appears at 8.828 keV and 9.278 keV, respectively.

4.2 RXTE

All our RXTE data used to deduce the spectra are corrected for dead-time.(this is the time when the detector is occupied with processing an event. During this time incoming photons are not processed and are lost; this is corrected by a model). The spectra of the two RXTE instruments (PCA and HEXTE) were combined in order to get spectra covering a wide energy band (3.5-200.0 keV). The combination of the PCU2 and HEXTE data resulted in 101 spectra spread over some 200 days and covering the whole outburst. The first selection of spectra covered the whole outburst at somewhat regular intervals. After modeling, this first selection uncovered

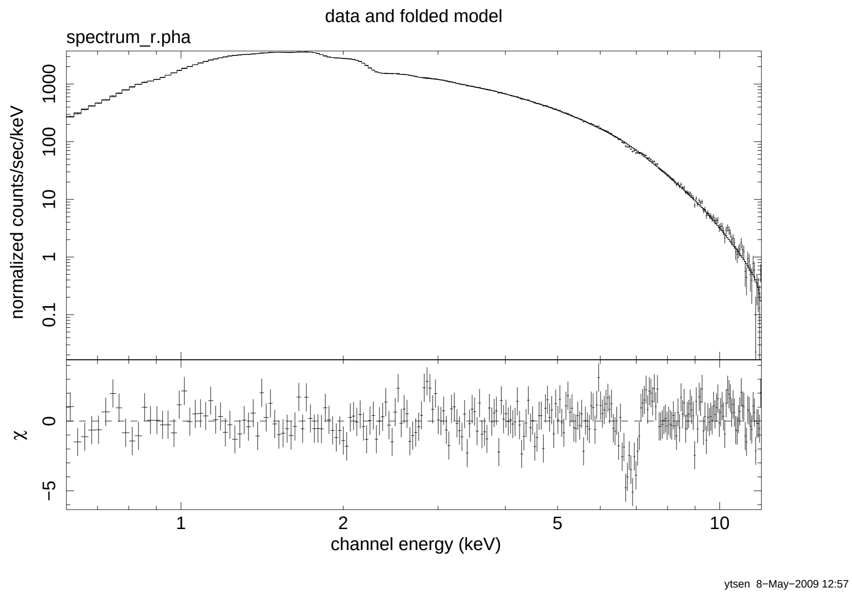

Figure 3: An example spectrum of a EPIC-PN observation, notice the iron lines at 6.7 and 6.97 keV.

Observation Date (MJD)	RAWX Source	RAWX Background	Pattern	Flag
53428	30-43	4-25:46-61	<5	0
53443	29-42	2-24:47-63	<5	0
53444	29-42	1-23:47-63	<5	0
53445	30-41	2-25:46-63	<5	0
53447	29-42	2-23:48-63	<5	0
53456	29-43	2-24:48-63	<5	0

Table 1: Spectral analysis info for EPIC-PN observations.

some periods of interest which required some closer inspection. This motivated us to sample some periods more thoroughly and therefore the 101 spectra are not selected at regular intervals.
The spectra were extracted from the data using the **runpcu2** and **runhexte** programs which were given to me by my supervisor, Mariano Mendez. These programs extract the source and background spectra for the PCU2 and HEXTE data respectively, so the spectra are background subtracted. These programs also produce response and ancillary matrices needed for the fits (see section 4.4 for details). The combined spectra of the PCU2 and HEXTE are fitted using XSPEC over the energy range 3.5-200 keV. The lower and upper energy limit was used because the calibration of the PCU2 below 3.5 keV and HEXTE above 200 keV is too uncertain.
The combined spectra of PCA and HEXTE were fitted using the XSPEC components **constant**, **diskbb** and **powerlaw**. We used the component **constant** to model the PCA and HEXTE spectra as one, taking into account the systematic differences in the calibration of the relative effective area of the instruments. The value of this component always stayed in a small range (0.75-1.00), which corresponds to a maximum difference of 25% between instruments. In a small percentage of spectra ($\sim$5%), a cutoff version of the power law was needed to get a good fit, in the other spectra the cutoff, if present, was located beyond 200 keV. In two cases a broken power law resulted in a better fit. Some models provided a better fit if we added a **gaussian** around 7 keV, representing a broadened iron line, or an **edge** at around 9 keV, representing an iron K-edge (for an example spectrum, see figure 4).

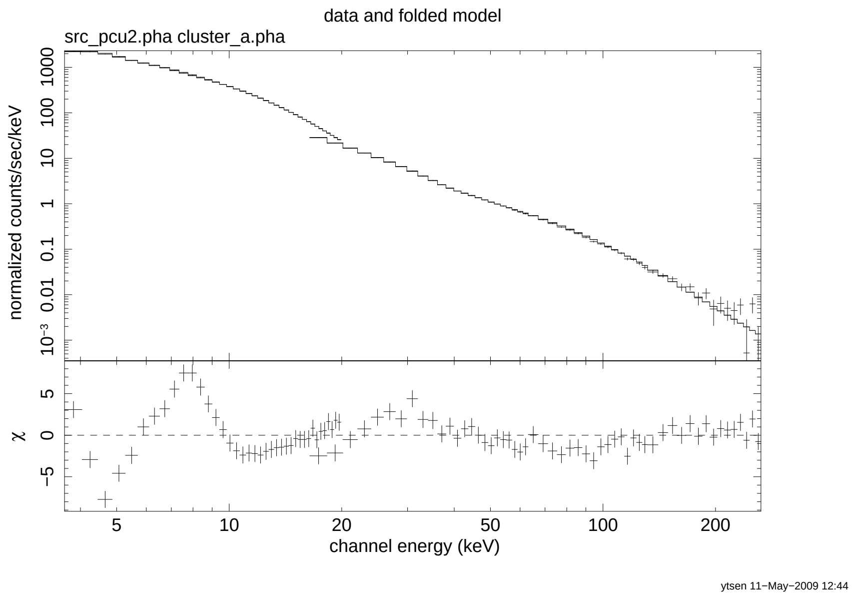

Figure 4: An example spectrum of a PCA and HEXTE observation.

4.3 Xspec Model Components

- **constant**: An energy-independent multiplicative factor. Used to match the spectra of the PCU and HEXTE instruments in order to be able to model the two spectra as a whole. The mismatch of the spectra is due to the systematic differences in the calibration of the relative effective area of the instruments.

- **phabs**: Absorption due to interstellar material along the line of sight.

$$M(E) = exp[-n_H \sigma(E)]$$

  Par1 = n_H: hydrogen column density
  σ(E) is the photo-electric cross-section (Excluding Thomson scattering)

- **diskbb**: The spectrum from an accretion disk consisting of multiple blackbody components.
  Par1: temperature of the inner-disk radius (keV)
  Norm

$$\left(\frac{(R_{in}/km)}{(D/10kpc)}\right)^2 cos(\theta)$$

,where R_{in} is the inner disk radius, D is the distance to the source, and θ is the inclination angle of the accretion disk (θ=0° is face-on). The inferred inner disk radius is corrected later in order to take into account the Comptonizing properties of the atmosphere of the disk.

- **powerlaw**: this is a simple photon power law.

$$A(E) = KE^{-\alpha}$$

par1 = α: photon index of the power law (dimensionless).
Norm = K: #photons $keV^{-1}cm^{-2}s^{-1}$ at 1 keV.

- **bknpower**: A broken power law.

$$A(E) = \begin{cases} KE^{-\Gamma_1} & E \leq E_{break} \\ KE_{break}^{\Gamma_2-\Gamma_1}(E/1keV)^{-\Gamma_2} & E \geq E_{break} \end{cases}$$

par1 = Γ_1: power law photon index for $E \leq E_{break}$
par2 = E_{break}: break point for the energy in keV
par3 = Γ_2: power law photon index for $E \geq E_{break}$
Norm = K: #photons $keV^{-1}cm^{-2}s^{-1}$ at 1 keV.

- **cutoffpl**: A power law with a high-energy exponential rolloff.

$$A(E) = KE^{-\alpha}exp\Big(-\frac{E}{\beta}\Big)$$

par1 = α: power law photon index
par2 = β: e-folding energy of exponential rolloff (in keV)
Norm = K: #photons $keV^{-1}cm^{-2}s^{-1}$ at 1 keV.

- **gabs**: A Gaussian absorption line.

$$M(E) = exp\Bigg(-\Bigg(\frac{par3}{\sqrt{2\pi}par2}\Bigg)exp\Bigg(-.5\Big(\frac{(E-par1)}{par2}\Big)^2\Bigg)\Bigg)$$

par1: line energy in keV
par2 = σ: line width in keV
par3: optical depth

- **gauss**: A simple Gaussian line profile. If the width is ≤ 0, it is treated as a delta function.

$$A(E) = K\frac{1}{\sigma\sqrt{2\pi}}exp\bigg(-\frac{(E-E_l)^2}{2\sigma^2}\bigg)$$

par1 = E_l: line energy in keV
par2 = σ: line width in keV
Norm = K: # photons $cm^{-2}s^{-1}$ in the line

- **edge**: An absorption edge.

$$M(E) = \begin{cases} 1 & E \leq E_c \\ exp\Big(-D(E/E_c)^{-3}\Big) & E \geq E_c \end{cases}$$

par1 = E_c: the threshold energy
par2 = D: the absorption depth at the threshold

- **laor**: An emission line from an accretion disk around a black hole (A. Laor, ApJ 376, 90).
par1: The line energy in keV
par2 = α: power law dependence of emissivity (scales as $R^{-\alpha}$)
par3: the inner radius of the accretion disk (in units of $R_g = \frac{GM}{c^2}$)
par4: the outer radius of the accretion disk (in units of $R_g = \frac{GM}{c^2}$)
par5: the inclination of the accretion disk (in degrees)
Norm: # photons $cm_{-2}s^{-1}$ in the line

- **warmabs**: An analytic model to calculate spectra due to a photoionized absorber.
par1 = the warm absorber column density in cm^{-2}.
par2 = The ionization parameter in log.
par 3-12 = The abundances of Ca, Na, O, Ne, Mg, Si, S, Ar, Ca and Fe with respect to solar abundances.
par 13 = Turbulent broadening in kms^{-1}.
par 14 = Redshift of the source.

4.4 X-ray Spectra Fitting With XSPEC

Due to the lower spectral resolution in comparison with optical telescopes, observed X-ray spectra have to be fitted by taking into account certain instrument dependant properties. The spectrometer of the X-ray telescope does not measure the actual spectrum, but photon counts (C) within specific channels (i). The actual spectrum $f(E)$ is related to the observed spectrum in the following way:

$$C(i) = \int_0^\infty f(E)R(i,E)A(E)dE$$

Where $R(i,E)$ is the instrumental response which is proportional to the probability that a photon with energy E is detected in channel i. $A(E)$ is the effective area of the instrument. Both these values are calibrated regularly and included with the requested data.
In practice this is not a continuous but a discrete process, defined in the following way:

$$S_i = C_i - B_i$$

The source spectrum S_i is the observed source spectrum C_i minus the background B_i.

$$D_i = \sum_{i=1}^{N} f_E R_{i,E} A_E$$

D_i is the spectrum resulting from the model you defined (f_E).
In XSPEC you will define a model f_E and use this as ansatz to check if this model in combination with the response and ancillary matrices result in a spectrum (D_i) similar to your observed spectrum (S). This is done via the χ^2 method:

$$\chi^2 = \sum_{i=1}^{N} \frac{(D_i - S_i)^2}{\sigma_i^2}$$

Where σ_i is the error in S_i. If your ansatz results in a low χ^2, the model gives a good description of your spectrum.
However, the fact that your model produces a good fit does not mean that it is the only good model, this is something the researcher has to decide.
This method seems somewhat time-consuming and could be simplified by using matrix multiplication to obtain the model. Considering the fact that the vectors D_i and A_E are known, as well as the matrix $R_{i,E}$, a simple multiplication of the inverse of A_E and $R_{i,E}$ with D_i would result in your model f_E. But unfortunately all the components come with errors, and these errors would propagate to huge errors in the model. This makes this method unsuitable for our needs.

5 Results

The spectra of XMM-Newton (EPIC-PN) and RXTE (PCA & HEXTE) were fitted with models described in sections 4.1, 4.2 and 4.3 using the algorithm described in section 4.4. These models resulted in good fits in most cases (for χ^2 of each observation, see section 8). The following results were obtained by using these models.

5.1 RXTE

The lightcurve of GRO J1655-40 over a period of about 14 years (October 1995 - April 2009) is plotted in Figure 5; this plot shows the count rate of the ASM instrument (2.0-12.0 keV) plotted against modified Julian day (MJD). The figure shows two outbursts of GRO J1655-40. Figure 2 shows the lightcurve of the 2005 outburst in detail. The hardness-intensity diagram (HID), which shows the ratio between the hard photons (6.0-20.0 keV) and the soft photons (3.0-6.0 keV), the so-called "hardness", and the total PCA count rate is plotted in Figure 6. The start of the outburst occurred around MJD 53439 which corresponds to the March 10 2005 and ended around MJD 53650 (October 7 2005), this means that the whole outburst had a duration of about 210 days. The lightcurve shows a double-peaked profile which also appears in the previous outburst (1996-1997) of this source (Sobczak et al. 1999) and the 1998-1999 outburst of the blackhole candidate XTE J1550-564 (Sobczak et al. 1999). The lightcurve and HID are plotted in six different colors which correspond to phases of the outburst which exhibit unique properties, the nature of these properties will become clear in the following sections. In phase I of the outburst the source is in the transition from the quiescent mode to the low/hard state judging by the low count rate in the lightcurve and the hardness of the spectrum. Figure 1 shows radio emission in this phase which can be connected to a wind emanating from the accretion disk (Rupen, Dhawan & Mioduszweski 2005). The first peak (phase II) corresponds to the transition from the low/hard state, in which the outburst began, to the high/soft state, as can be seen in the HID. This quite radical shift in hardness only took two days to complete. This phase also exhibits strong flaring in the radio which suggests the presence of a jet, this will be discussed in section 5.5. Phase III can be considered as the beginning of the second peak but shows some characteristics which deviate from the rest of the peak, this will be discussed in section 5.1.3. This phase shows an increase in flux in the ASM and PCA and steady state in hardness. phase VI shows a considerable increase in flux to peak values (10000 cnt/s PCA, 325 cnt/s ASM, ≈ 4 Crab). It also represents a short transition back to intermediate hardness in the peak and back to the soft state at the end. phase V shows a small bump in the lightcurve which is followed by

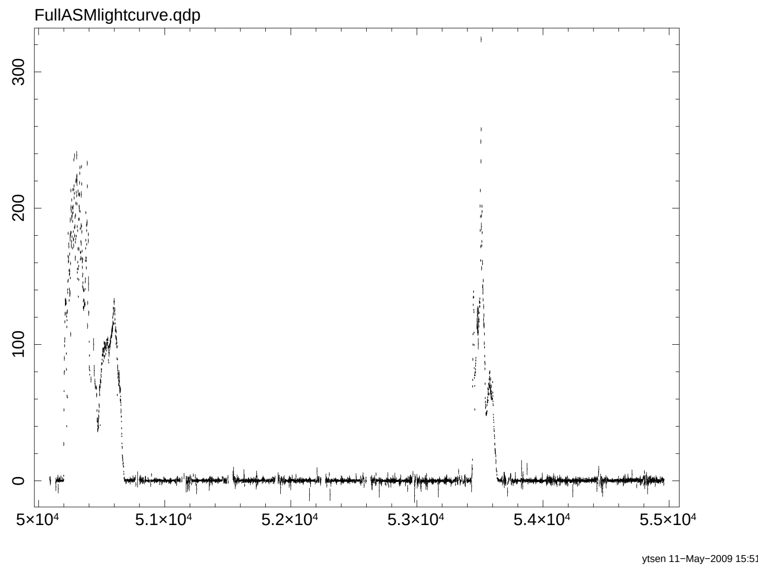

Figure 5: The ASM lightcurve of GRO J1655-40 from October 1995 to April 2009.

a steady decline in flux as well as some dynamic behavior in the HID, but still remaining in the soft part of the spectrum. Phase VI shows a transition back to the low/hard state and finally to quiescence. This transition takes a while longer (about a week) and happens at somewhat lower count rate values than the transition in phase II; this shows up in the HID as the well known but poorly understood hysteresis effect (Homan et al. 2001).

The canonical picture of X-ray binaries in outburst give some standard states that can be derived from the HID as described in the following sections. In the following sections I will treat each state identified in the HID in more detail using the lightcurve and some other parameters obtained from the models I have fitted.

5.1.1 Low/Hard State

This state is identified by a low flux, several orders of magnitude lower than during the peak of the outburst, and a hard spectrum. Sources like GRO J1655-40 reside in the quiescent state for most of their lifetime and move to the low/hard state at the beginning and the end of the outburst. This state is represented by phases I and VI in our HID. The canonical picture of the geometry of the source during this state shows a very weak or even the absence of an accretion disk around the compact object; this results in a spectrum that is dominated by a power-law feature which can be connected to a hot comptonizing cloud ($T_e \sim 100$ keV) up-scattering photons. This

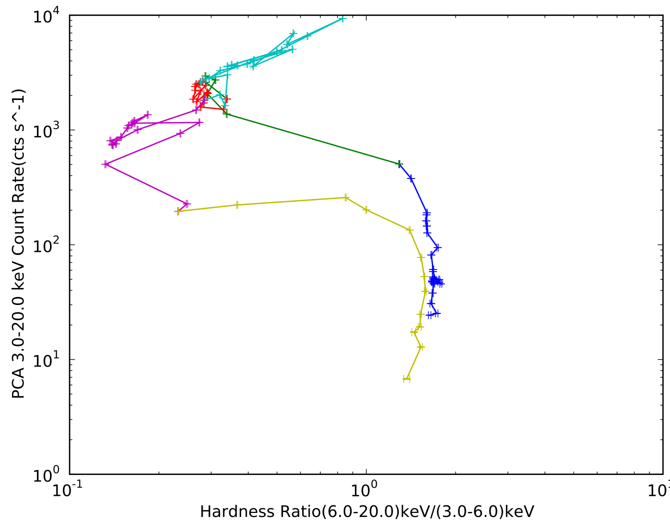

Figure 6: The hardness-intensity diagram.

appears to be confirmed by Figure 7, which shows that the disk blackbody flux is negligible and that the power-law flux dominates in phases I and VI. Considering the fact that the disk is not significant, the contributions to the figures which show the effective inner radius of the accretion disk and the effective temperature can be ignored in these two phases. The photon index, which represents the steepness of the power law, lies around 1.5 in this state; this also agrees with the classical picture.

5.1.2 High/Soft State

The first peak (phase II) of the lightcurve is the transition between the low/hard state and the high/soft state and phase V represents the reverse transition. As the name suggests, this state can be identified by a high flux and a soft spectrum. In the canonical picture, the soft spectrum is attributed to an increase of soft photons from an optically thick, geometrically thin accretion disk around the black hole. This is confirmed by figure 7 which shows that the disk contributes 50-100% of the total flux in phases II, III and V. Also an increase in disk temperature (from 0.6 to 0.8 keV) and a decrease in effective radius (from $7R_g$ to $2.5R_g$, $R_g{=}\frac{GM}{c^2}$) in phases II and III indicate that the accretion disk is growing closer to the compact object and vice versa in phase V. From the canonical picture of black hole states (e.g. Mendez & van der Klis 1997) it is expected that the photon index in the high/soft state lies around 2.5. This is the case in phase V but phases II and III show strong deviations from the standard picture, with a rapid

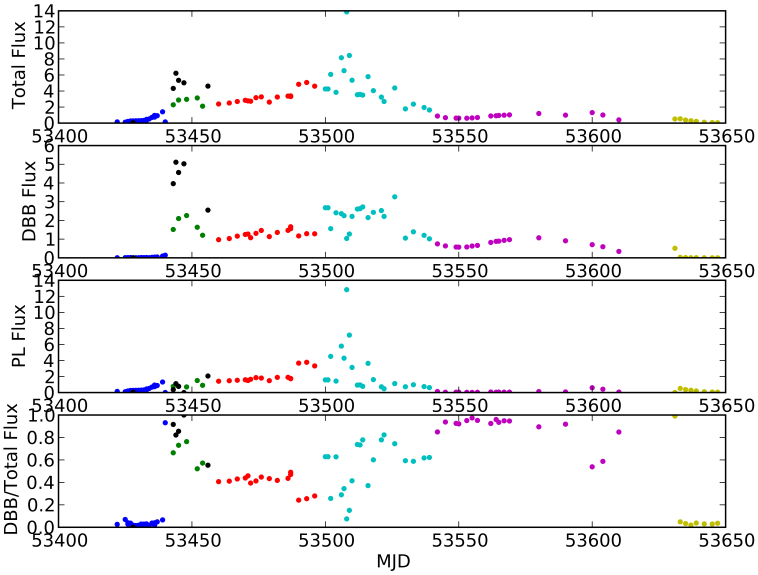

Figure 7: The flux has units of 10^{-8}erg $cm^{-2}s^{-1}$. The black dots represent XMM-Newton:EPIC PN-data.

increase of the power-law photon index from 2 to 5 in phase II and a steady value of around 6 in phase III. These values of the photon index in phase III are unusually high and therefore this phase is very interesting and will be treated in more detail in section 5.1.3.

5.1.3 Super Soft State

Phase III, which is situated between the two peaks in the lightcurve, shows some strange developments compared to the standard picture. Some of the parameters like power-law photon index (Γ), R_{eff} and power-law flux appears to deviate from the overall trend as was mentioned in the previous section. Especially the photon index in this phase stands out from the rest of the outburst as is clearly seen in Figure 8. This phase shows a rapid increase in Γ (from 1.5 to 6). Figure 8 shows that the photon index in phase III is very high ($\Gamma \sim 6$) compared to the rest of the outburst ($1 \leq \Gamma \leq 3$). In this phase the power law contributes some 50% of the total flux and the overall count rate in the lightcurve is higher then 2000 counts/s/PCU ($\approx$1 Crab). The significant contribution of the power law to the total flux and the high count rate indicate that the high photon index is not the result bad statistics. The fact that the photon index increased continously from $\sim$1.5 to $\sim$6 in phase II, and was always consistantly around 6 in phase II indicates

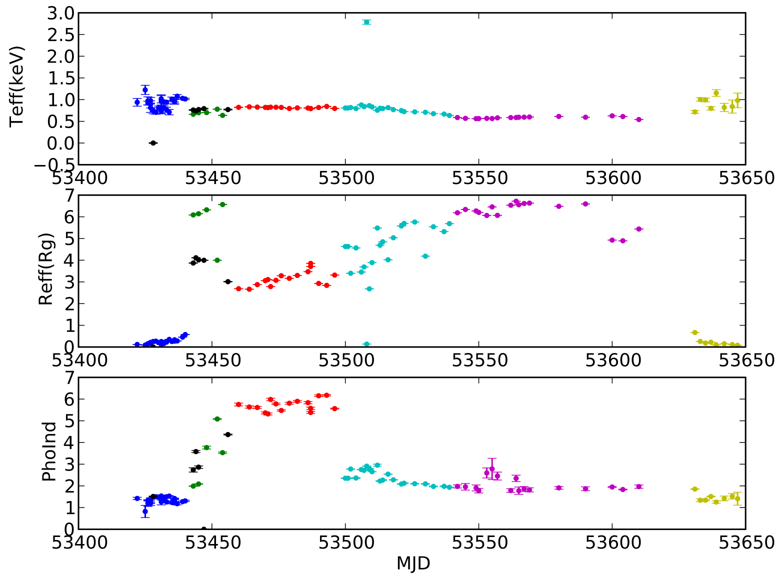

Figure 8: The black dots represent the XMM-Newton:EPIC-PN data.

that the change is real, and is not due to a malfunction of the instrument. On the other hand, it is highly unlikely that this extremely high photon index is a result of a physical phenomenon. A more plausible explanation is that the components used to model the data do not work in this instance, which indicate that there is something unusual happening during this phase. The R_{eff} and T_{eff} seem to be quite stable during phase III, none of these parameters show unusual values in this phase. T_{eff} lingers around 0.8 keV and R_{eff} slowly increases from around $3R_g$ to $4R_g$. The total flux increases slightly with equal contribution of the disk and the power-law component, but at the end the power-law component becomes the dominant factor.

5.1.4 Very High State

Phase IV is designated as the very high state, but its short deviation to intermediate hardness values make it a somewhat anomalous state. This phase is represented in the ASM lightcurve by the highest peak, reaching up to a flux of ≈ 4 Crab (a typical X-ray source has a flux of about 0.1 Crab, whereas the brightest X-ray source in the sky, with exception of the Sun, reaches a flux of about 11 Crab (Sco X1)). The hardness ratio diagram shows a peak in the PCA count rate and a short deviation from the soft to an intermediate state. This deviation suggests a decrease in the contribution of thermal (soft, disk blackbody) emission to the overall flux. This is supported by Figure 7 which shows that the power-law contribution becomes more important around the peak. The beginning and the end of this phase shows a somewhat erratic development in the flux contributions. This is also the case when we look at the R_{eff}; it varies day by day from the unphysical value of around zero at the peak flux ($R_{eff} > 1.23R_g$ for maximally rotating Kerr blackhole, $R_g = \frac{GM}{c^2}$) to values as high as $6R_g$ at the end. The temperature shows a steady increase from 0.8 keV to 0.9 keV towards the peak and a decrease to 0.6 keV at the end. But at the peak of the outburst the temperature shoots up to 2.6 keV; this datapoint corresponds to the very low value of R_{eff}. The extreme values in temperature as well as inner radius at the peak of the outburst suggests that the physics used in the model components fall short at this point. But we can assume that this point represents the highest value in temperature and the lowest inner radius value. The photon index has returned to familiar values in this phase ($\Gamma \sim 2.5$).

5.2 Parameter Correlations

Figures 9 and 10 show the luminosity in Eddington units ($L_{edd} = 8.78 \times 10^{38}$ erg s^{-1}, for M = 7.02$M_{\odot}$) versus R_{eff} (in R_g) and Γ. Figure 10 shows a clear correlation between the luminosity and Γ, with the exception of phase III and partly phase II which clearly deviate from the overall trend. The trend indicates that an increase in luminosity results in an incease in photon index; it must be added that this trend is heavily supported by the data of phase IV. The luminosity peaks in phase IV at 10% of Eddington, the other phases seem to have lumonisity values below 3% Eddington.

Figure 9 indicates that an increase in luminosity results in a decrease in R_{eff}; phase III again deviates from this overall trend (the deviation of phases I and VI were to be expected due to the insignificance of the disk in these phases, this is also the case in figures(11&12)). With the exception of phases I, III and VI, the anti-correlation between the luminosity and R_{eff} is quite good and close to linear.

Figures 11 and 12 show T_{eff} (in keV) and the power-law flux (in 10^{-8}erg s^{-1} cm^{-2}) versus R_{eff}. Figure 11 shows that a decrease in R_{eff} corresponds to an increase in power-law flux. Figure 12 shows that as the accretion disk moves in, the temperature rises, this is in accordance with the canonical model of an outburst.

5.3 Model Parameters

From the RXTE models a couple of parameters can be deduced that give a clearer picture of the development of the source during the outburst. The **diskbb** component gives the apparent temperature at the inner disk radius

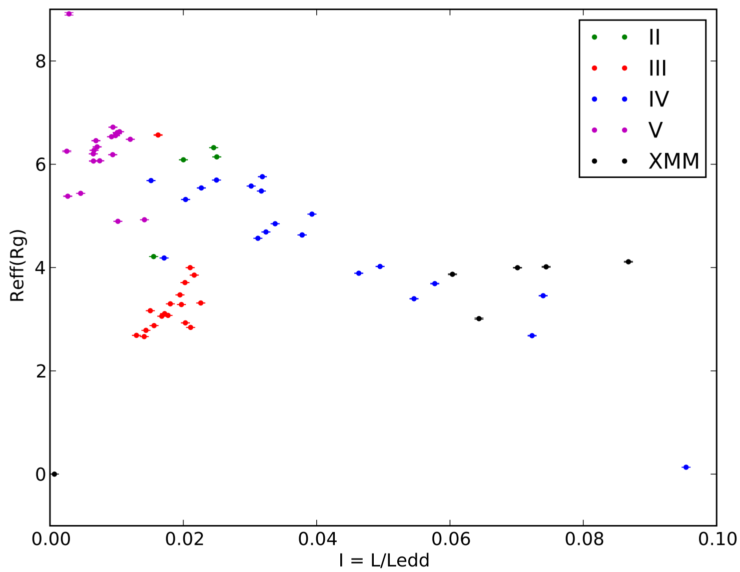

Figure 9: Plot of R_{eff} against Luminosity in Eddington units ($L_{edd} = 8.8 \times 10^{38}$erg s^{-1}, for M = $7.02 M_{\odot}$).

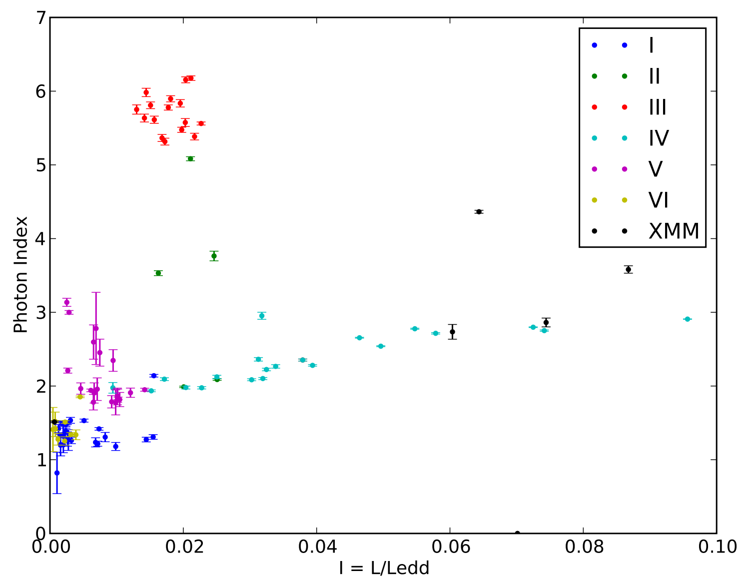

Figure 10: Plot of Photon Index against Luminosity in Eddington units.

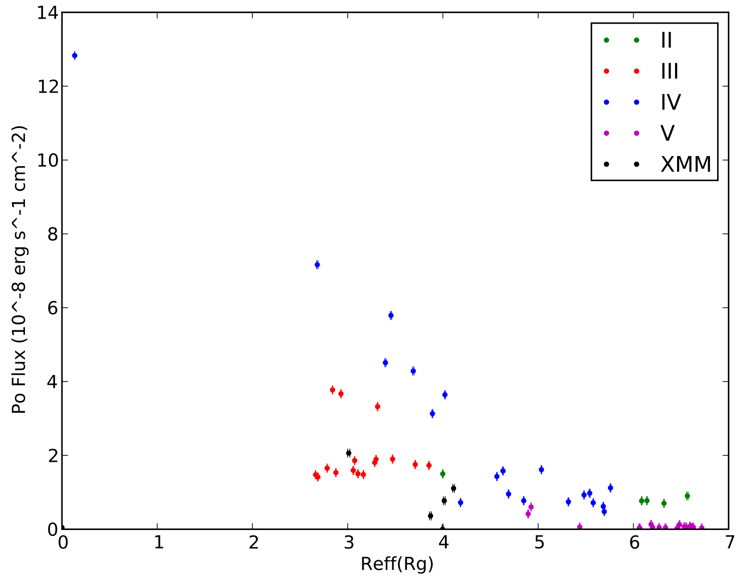

Figure 11: Plot of power-law flux against R_{eff}.

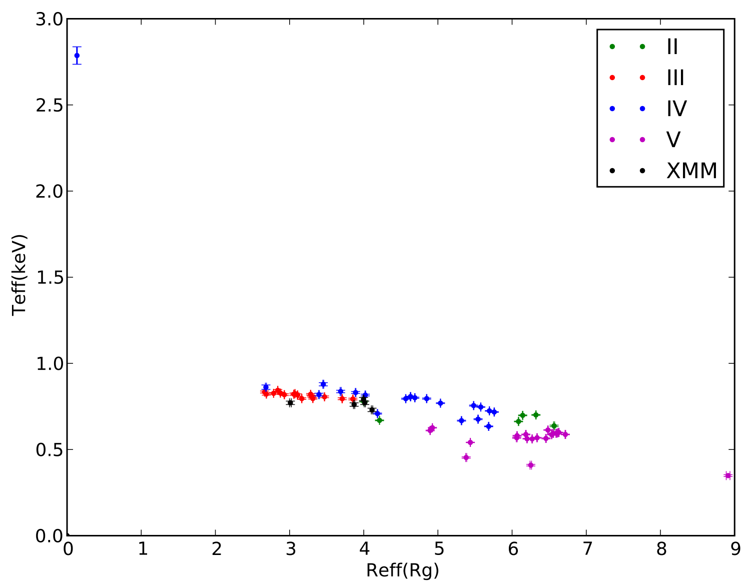

Figure 12: Plot of T_{eff} against R_{eff}.

and the normalization of this component. The definition of the normalization includes the distance to the source, the inclination of the source and the inner disk radius (see section 4.3). As the distance to and the inclination of GRO J1655-40 are quite well measured (D = 3.2 ± 0.2 kpc, i = $69.5°$), the inner radius of the disk can be calculated. The fitted inner disk radius and inner disk temperature are not the same values as the effective radius and temperature used in Figures(8 & 12); are corrected for Comptonization in the disk atmosphere. This correction is needed when electron scattering just above the disk is the dominant source of opacity and affects the inner disk spectrum through Comptonization. The Comptonized disk spectrum appears to be hotter than it actually is, and therefore we need to correct the observed values to obtain the temperature and radius of the disk. A diluted blackbody is often used to correct for this phenomenon which results in a spectral hardening factor f for the radius and temperature. Shimura and Takahara (1995) have used numerical simulations to calculate this factor and concluded that it can be approximated by a constant $f = 1.7 \pm 0.2$. This hardening factor is defined in such a way that $T_{eff} = \frac{T_{in}}{f} = \frac{T_{in}}{1.7}$ and $R_{eff} = f^2 R_{in} = 2.9 R_{in}$, where T_{in} and R_{in} are the values obtained from the fits.

The **powerlaw** component represents the high energy tail of the spectrum due to up-scattered photons from the disk. This means that the power law provides us with an insight into the corona of electrons which surrounds the source. The power-law component gives us the norm which is coupled to the flux and the photon index which represents the steepness of the power law. These two parameters are essential in understanding the significance of the corona and its connection to the disk.

5.4 XMM-Newton

The six observation of XMM-Newton lie in phase II of the outburst, which corresponds to the first peak and the transition from the low/hard state to the high/soft state. These six observations give us an opportunity to use two independent instruments of different resolution and coverage to get a more extensive picture of this phase in the outburst. The numerous observations of RXTE give an insight of the overall behavior of the disk and the surroundings through several of its parameters as was shown in the previous sections. With the six high resolution XMM-Newton spectra we can use absorption features to get an insight into the morphology of the ionized gas around the accretion disk.

The effective temperature of the inner disk seems to be quite steady during the six XMM-Newton observations. The effective inner radius shows a decreasing trend as does the disk blackbody flux towards the end; this coincides with an increasing power-law flux and power-law photon index.

Observation Date	Optical Depth FeXXV	Optical Depth FeXXVI	Optical Depth NiXXVIII
53443	7.18E-03±6.0E-03[a]	7.08E-02±5.0E-03	4.26E-02±1.0E-02
53444	3.99E-02±6.1E-03	2.86E-02±5.0E-03	3.56E-02±1.13E-02[a]
53445	1.79E-02±4.5E-03	2.97E-02±4.5E-03	2.98E-02±1.0E-02
53447	4.98E-02±4.0E-03	4.02E-02±2.65E-03	2.07E-02±5.5E-03
53456	3.58E-02±3.0E-03	1.96E-02±6.2E-03	5.96E-03±1.0E-03[a]

Table 2: [a]These values are upper limits.

This was to be expected in a transition from the low/hard to the high/soft state. The values of T_{eff} and R_{eff} obtained from the XMM-Newton data are comparable with the RTXE data at similar observation dates.
In four of the six observation the spectrum was fitted using a **diskbb** and a **powerlaw**; the first observation does not require a disk component and the fifth observation does not need a power law. The fact that EPIC-PN instrument extends only up to 12 keV diminishes the need for a power law. In every spectra but the first, at least one highly ionized iron absorption line was found; in observation two only the FeXXVI line and in the other four also the FeXXV line. Also an absorption line at 8.08 keV, representing NiXXVIII, was detected in observations two, four and five. The optical depth of the FeXXVI line peaked at the second observation ($\tau \approx 7\times10^{-2}$) and assumed lower values at the rest of the observations ($2\times10^{-2} < \tau < 4\times10^{-2}$). The optical depth of the FeXXV line fluctuated between 1.8×10^{-2} and 5×10^{-2}. For observation two an upper limit for the optical depth of FeXXV was calculated ($\tau = 7.18\times10^{-3}$). For the exact values of the optical depth of all the ions at all observations, see Table 2.

5.5 Radio Emission

Figure 1 shows the emission of GRO J1655-40 in radio at different frequencies (Rupen, Dhawan & Mioduszewski 2005). As previously mentioned, this source had radio jets (Hjellming & Rupen 1995; Tingay et al. 1995). The radio emission of these jets can clearly be seen in the Figure. The radio emission is concentrated in phases I, VI and especially II. This corresponds to the empirical picture that there is continuous and steady radio emission in the low/hard state, whereas around the state transition from hard to soft, strong radio flares are detected (Fender, Homan & Belloni 2009).

6 Discussion

This analysis of the 2005 outburst of X-ray transient GRO J1655-40 has uncovered an unprecedented state characterized by a very steep power law ($\Gamma \approx 6$). This is the first time such a super soft outburst state has been observed in about two dozen X-ray transients. This unusual state clearly does not fit in the pre-existing classifications of black-hole states, and could represent a new addition to the canonical scenario.

In addition, an extremely high flux data point has been observed at the very peak of the outburst. This extremely high flux peak has not been observed in previous outbursts of this source and only once in another X-ray transient (XTE J1550-564, Sobczak et al. 1999). This point represents extreme circumstances in the inner radius of the accretion disk and can not be described by the physics assumed in the **diskbb** model of XSPEC. This point only lasted for one day, and this could be the reason it is not observed in more X-ray transients.

The analysis of the XMM-Newton (EPIC-PN) and RXTE (PCA & HEXTE) data provide a complete overview of the 2005 outburst of GRO J1655-40. The overall behavior of the source agrees with the canonical scenario to a certain extent. As is described by the canonical model (section 2.2), the source started out in the low/hard state. The morphological situation during this state can be interpreted as a weak and cool disk emitting soft photons, which are partly up-scattered by a hot corona surrounding the black hole. During this state GRO J1655-40 is emitting in the radio as well as in X-ray. This could indicate the presence of a radio jet or wind in the low/hard state; this is supported by observations of other sources (Fender, Homan & Belloni 2009). The next phase in the outburst, phase II, is represented by a local peak in the lightcurve. This phase is identified as the high/soft state and is covered by both RXTE and XMM-Newton observations; I will discuss the XMM-Newton results in section 6.1. In this phase the contribution of the accretion disk becomes stronger, and its inner radius starts to move closer to the black hole. The photons received during this phase are rapidly becoming softer, indicating that the growing disk is producing increasing amounts of soft photons. This phase also shows an increase in radio emission, which is an indication of the presence of a strong radio jet. This jet could be formed from the radio flow in phase I, or replaces it by blowing it away. Phase II also shows a steady increase in photon index to very high values ($\Gamma \sim$5) as the source moves into phase III. Phase III was called the super soft state, and clearly deviates from the canonical picture because of a very high photon index. The power law is significant in this phase, therefore these photon index values cannot be dismissed as being the result of bad statistics. But what these extreme values mean is a matter of debate. The high photon-index values are probably due to changes in the corona or the disk. It could be that these changes mean that the physics

used in the fitting components of XSPEC, especially the **powerlaw**, are not adequate anymore and therefore give us these anomalous values. The other option is that the observed values are real and the consequence of significant changes in the comptonizing material. The disk could have become geometrically thick (e.g. due to a sudden increase in $\dot{M}$). This change in the geometry of the disk could also affect the properties of the surrounding corona. The thick disk produces more photons that can be up-scattered by the corona. The transference of energy to these photons cools the corona, hampering it to up-scatter the large amount of soft photons from the thick disk. This would reduce the contribution of hard photons in the spectrum, steepening the power law. An indication of an increase of the optical depth of the corona is the sudden decrease in variability in phase III. This phase shows an rms variability of about 5%, whereas in the surrounding phases the variablilty has values of 10% or more (B.Hiemstra, private communication). This suggests that in phase III the variable signals, probably originating from the inner radius of the accretion disk, are scattered in the surrounding medium and/or the thick disk and subsequently loose their variablility.
Phase IV shows a peak in both the total flux and the disk temperature and is therefore designated as the very high state. At the top of this peak the temperature reaches about 2.7 keV and the inner radius is almost zero R_g. These values are unphysical; the temperature is extremely high and R_{eff} would be inside the inner most stable orbit of a maximally rotating black hole (R $= 1.23R_g$). This is an extreme point in the outburst, but the physics assumed to fit the spectrum are probably falling short here, therefore the values of T_{eff} and R_{eff} at this point should be taken with caution.
In the HID, the hardness at the peak of the outburst deviates to intermediate values in phase IV. This deviation includes a significant amount of points around the peak, and is not only supported by the extreme point mentioned before. The origin of this increased hardness could be traced back to a Comptonizing cloud present in the line-of-sight, which either moves away after a couple of days or is cooled to a temperature which is not sufficient for Comptonization anymore.
Phase V includes the transition from the high/soft state to the low/hard state, only at a lower flux than the inverse transition in phase II. Phase VI represents the end of the outburst and the transition back to quiescence.
As said before, the absorption lines present in the majority of the XMM-Newton spectra can be used to map the geometry of the ionizing medium surrounding the source. The following section will elaborate on the methods used to get a picture of the geometry of the system.

6.1 Iron Line Ratio

The comparatively high resolution of the XMM-Newton spectra gives us an opportunity to use absorption features to get a picture of the geometry of the ionizing medium surrounding the source. In most of the XMM-Newton spectra absorption lines are observed at 6.7 and 6.97 keV (Figure 3). These lines indicate the presence of highly ionized FeXXV and FeXXVI atoms in the ionized corona. We observe these features because the accretion disk photons and the photons that get scattered of the corona encounter an absorbing medium in the vicinity of the source on the way to our instruments. In order to put these data to good use we have to calculate the ionization parameter ξ of this gas. This parameter is defined as: $\xi=\frac{L}{n_e r^2}$ (X-Ray Spectroscopy in Astrophysics, van Paradijs & Bleeker 1997 hereafter XRSA), where L is the luminosity of the ionizing source, n_e the electron density in the ionized gas, and r the distance between the ionizing source and the gas. The ionization parameter can be calculated using the ratio of the optical depth of the two lines (τ_{FeXXV} and τ_{FeXXVI}), the cross section of these atoms (σ_{FeXXV} and σ_{FeXXVI}), the radiative recombination rate (α), ϕ, which is related to the photoionization rate β, and the collisional ionization rate C in the following way (see XRSA, pg 215 eq. 122):

$$\xi = (\alpha_{i+1}\frac{\tau_{FeXXVI}}{\tau_{FeXXV}}\frac{\sigma_{FeXXV}}{\sigma_{FeXXVI}} - C_i)/\phi_i$$

The luminosity of the source can be derived from the data, so $n_e r^2$ can be calculated.

Assuming a certain geometry for the ionized region (e.g. like a spherical region with constant density), we can derive the product of n_e and r. In the process of this calculation we have to make a couple of assumptions which can have some influence on the eventual results. The product of n_e and r, assuming a constant n_e in a spherical region, is equal to the electron column density N_e. The ratio between the optical depth of a line (τ_{FeXXV}) and the cross-section of this ion (σ_{FeXXV}) is equal to the column density of this ion (N_{FeXXV}). This ion column density can be converted to the total column density by multiplying it by the abundance of iron in this region and the fraction of FeXXV to the total amount of iron. If we assume that the electron density is equal to the equivalent hydrogen density, we can calculate $n_e r$ in the following way:

$$n_e \times r = \frac{\tau_{FeXXV}}{\sigma_{FeXXV} \times f \times A}$$

Where f is the fraction and A the abundance.

Considering the fact that $n_e \times r^2 = \frac{L}{\xi}$, we can deduce the electron density and the radius of the ionizing region. For these calculations we computed the values for the photoionization cross-section (σ) using the methods and data from Verner et al. (1996) and the radiative recombination rates (α)

were taken from Verner and Ferland (1996). The abundance of iron in the absorbing material was set equal to the abundance in the Sun (Verner et al. 1996) and the fraction of FeXXV and FeXXVI was deduced from a charge state abundance plot assuming an ionization parameter of 4 (Sako, private communication), which is more or less typical for our fits (see Table 3). ϕ was calculated using the formulas from XRSA (pg 215 eq. 117 & 118) and the collisional ionization rate (C) was set to $3.0 \times 10^{-16}\mathrm{cm}^2\mathrm{s}^{-1}$ (XRSA, pg. 216). The product of these assumptions can influence the results by a few order of magnitudes. In order to get an indication of the significance of these results, we have used an independent method of getting these parameters. The above calculations involve a number of simplifying assumptions. In order to get more accurate figures for the physical parameters of the ionized material, we proceed as follows.

We included the Xspec component **warmabs** described in section 4.3 to our fits. This component replaces all individually fitted absorption lines with one single absorbing component. The fit with this model component gives the ionization parameter and the density of the region, assuming the element abundances in the region are solar (the abundances can be changed, but with lack of a better assumption, I used solar). This method gives similar values as in a comparative research (van Peet et al. 2009) and differ from the first, very crude, method by factors of a few. The results using **warmabs** are given in table 3, the model is a sphere of radius R with constant density.

The results presented in Table 3 show that for both models the density and the radius/distance remain more or less constant during the five observations. The sphere model shows that the ionized cloud starts out quite close to the source and at high density (Obs. A). After that the cloud recedes and drops in density for one day (Obs. B), but slowly approaches the source again with increasing density (Obs. C, D & E).

Acknowledgments.. I want to thank my supervisor, Mariano Mendez, for investing a lot of time into this research and for answering numerous questions. I would also like to thank Beike Hiemstra for providing me with very usefull data and helping me from time to time.

FeXXV					
Observation	Model	log(ξ)	NH($10^{22}cm^{-3}$)	r(10^{10}cm)	n($10^{10}cm^{-2}$)
A MJD 53443	Sphere (r=R)	4.00±0.06	1.25±0.12	13.39±1.29	9.34±1.79
B MJD 53444	Sphere (r=R)	3.84±0.12	1.00±0.15	22.93±3.44	4.36±1.31
C MJD 53445	Sphere (r=R)	4.06±0.19	1.05±0.19	16.52±2.99	6.36±2.30
D MJD 53447	Sphere (r=R)	4.00±0.07	1.37±0.04	15.74±0.46	8.71±0.51
E MJD 53456	Sphere (r=R)	3.81±0.09	1.22±0.09	15.16±1.12	8.05±1.19

Table 3: The results of the fit using **warmabs** for FeXXV.

7 References

- Zhang,S.N.,et al.1994,IAU Circ. 6046
- Orosz,J.A. and Bailyn,C.D. 1997,ApJ,477,876
- Sobczak,G.J.,et al. 1999,ApJ,520:776-787
- Smith,D.M., Heindl,W.A., Swank,J., Leventhal,M., Mirabel,I.F., and Rodriguez,L.F. 1997, ApJ, 489, L51
- Hjellming, R. M., and Rupen, M. P. 1995, Nature, 375, 464
- Miller,J.M., Raymond,J., Reynolds,C.S., Fabian,A.C., Kallman,T.R., Homan, J.,2008ApJ...680.1359M
- Tingay, S. J., et al. 1995, Nature, 374, 141
- Fendt,C.,2006ApJ...651..272F
- Fender,R.P., Homan,J.,Belloni,T.M.,arXiv:0903.5166v1
- Rupen, Dhawan and Mioduszweski, 2005a ,Astronomer's Telegram 419
- Rupen, Dhawan and Mioduszweski, 2005b ,Astronomer's Telegram 425
- Rupen, Dhawan and Mioduszweski, 2005c ,Astronomer's Telegram 434
- Rupen, Dhawan and Mioduszweski, 2005d ,Astronomer's Telegram 437

- Rupen, Dhawan and Mioduszweski, 2005e ,Astronomer's Telegram 441
- Rupen, Dhawan and Mioduszweski, 2005f ,Astronomer's Telegram 443
- Rupen, Dhawan and Mioduszweski, 2005g ,Astronomer's Telegram 489
- Rupen, Dhawan and Mioduszweski, 2005h ,Astronomer's Telegram 609
- McClintock,J.E. and Remillard,R.A.,2006, in Compact Stellar Sources
- Arnaud,K.A., 1996ASPC..101...17A
- Shakura,N.I., Sunyaev,R.A.,1973AA....24..337S
- Sobczak,G.J.,et al. 1999,ApJ,517:L121-L125
- Homan,J.,2001ApJS..132..377H
- Mendez, M., and van der Klis, M. 1997, ApJ, 479, 926
- Shimura, T., and Takahara, F. 1995, ApJ, 445, 780
- van Paradijs,J. and Bleeker,J.A.M., X-ray Spectroscopy in Astrophysics, EADN School X Amsterdam, 1997
- Verner,D.A. and Ferland,G.J., ApJ,Suppl.Ser.,103:467-473,1996 April
- Verner,D.A.,et al., ApJ,465:487-498,1996 July
- van Peet,J.C.A,et al. arXiv:0902.4470v1

8 Appendices

8.1 XMM-Newton and RXTE Spectral Results

Obs. Date (MJD)	Obs. Time (s)	$\#N_H$ atoms ($10^{22} cm^{-2}$)	Disk BB T_{eff} (keV)	Disk BB[a] Flux (10^{-12} $ergcm^{-2}s^{-1}$	R_{eff} [b] (R_g)	Power-Law Photon Index	Power-Law[a] Flux ($10^{-12} ergcm^{-2}s^{-1}$)	χ^2_{red} (d.o.f.)
53428	42506	0.507±0.01	*	*	*	1.513±0.01	476.861±3.138	1.12 (256)
53443	15617	0.667±0.01	0.761±0.01	39639	3.870±0.009	2.735±0.10	3625.53±345.017	1.75 (253)
53444	15618	0.803±0.01	0.739±0.01	51098	4.112±0.009	3.581±0.05	11080.5±356.455	1.18 (250)
53445	15612	0.717±0.01	0.771±0.01	45611	4.014±0.009	2.862±0.06	7722.07±288.183	1.31 (248)
53447	23911	0.611±0.01	0.792±0.01	50256	3.997±0.006	*	*	1.90 (243)
53456	22335	0.913±0.01	0.771±0.01	25492	3.011±0.012	4.364±0.02	20623.6±218.440	1.85 (238)

Table 4: [a] The flux is measured between 0.5 and 12.0 keV. [b] R_{in} is calculated using a inclination of 69.5° and a distance of 3.4 kpc.

Obs. ID	Date (MJD)	Obs. Time (s)	$\#N_H$ atoms $(10^{22}cm^{-2})$	Disk BB T_{in} (keV)	Disk BB[a] Flux $(10^{-}12ergcm^{-2}s^{-1})$	R_{in} (km)	Power-Law Photon Index	Power-Law[a] Flux $(10^{-12}ergcm^{-2}s^{-1})$	χ^2_{re} (d.o
90058-16-02-00	53422	3411	3.28±0.82	0.94±0.01	38.415	0.04±0.01	1.42±0.05	1521.03±103.08	1.09 (
90058-16-03-00	53425	3401	2.97±0.51	*	*	*	1.66±0.02	1202.83±37.43	0.97 (
90058-16-04-00	53426	3514	2.52±0.81	1.68±0.15	68.656	0.04±0.01	1.16±0.15	1848.71	1.10 (
90428-01-01-00	53426	14129	3.19±0.57	1.55±0.15	52.902	0.05±0.01	1.42±0.08 (1)	206.39	1.16 (
90428-01-01-00							1.56±0.03 (2)		
90058-16-05-00	53427	2792	2.02±0.38	*	*	*	1.63±0.02	2268.65±51.82	1.10 (
90058-16-07-00	53427	3486	3.92±0.73	1.23±0.14	43.069	0.09±0.01	1.53±0.03	2845.78±106.00	1.08 (
90428-01-01-01	53427	3388	4.06±0.80	1.16±0.12	44.169	0.10±0.02	1.52±0.03	2719.84±99.60	0.82 (
90428-01-01-03	53428	3511	*	*	*	*	1.53±0.01	2780.06	1.19 (
90428-01-01-04	53429	13887	4.64±0.47	1.18±0.07	42.095	0.10±0.01	1.51±0.02	2982.99±60.22	1.42 (
90428-01-01-02	53430	12375	3.59±0.41	1.38±0.07	54.938	0.07±0.01	1.49±0.02	3093.75±65.90	1.37 (
90058-16-06-00	53431	1762	1.23±0.44	*	*	*	1.59±0.02	2459.49±69.91	1.07 (
90428-01-01-06	53431	2005	1.80±0.67	1.73±0.16	64.276	0.04±0.01	1.39±0.04	3156.38±153.75	1.01 (
90428-01-01-07	53431	2785	5.34±0.80	1.28±0.13	48.820	0.08±0.01	1.49±0.03	2817.74±119.05	0.93 (
90428-01-01-08	53431	1937	5.01±0.89	1.32±0.18	44.933	0.07±0.01	1.53±0.04	2703.65±127.96	1.22 (
90428-01-01-05	53431	6800	4.04±0.59	1.21±0.09	45.205	0.09±0.01	1.51±0.03	2772.07±83.48	1.18 (
90428-01-01-09	53432	13897	4.30±0.43	1.32±0.08	45.024	0.07±0.01	1.52±0.02	2815.03±57.52	1.19 (
90428-01-01-10	53432	11357	3.39±0.40	1.39±0.07	62.060	0.07±0.01	1.47±0.02	3522.84±69.13	1.01 (

Table 5: [a] The flux is measured between 3.5 and 200.0 keV. $T_{in} = 1.7\times\ T_{eff}$ and $R_{in} = R_{eff}/2.9$.

Obs. ID	Date (MJD)	Obs. Time (s)	$\#N_H$ atoms $(10^{22}cm^{-2})$	Disk BB T_{in} (keV)	Disk BB[a] Flux $(10^{-}12ergcm^{-2}s^{-1})$	R_{in} (km)	Power-Law Photon Index	Power-Law[a] Flux $(10^{-12}ergcm^{-2}s^{-1})$	χ (d.
91404-01-01-00	53433	5758	*	*	*	*	1.52±0.01	3387.94±35.13	1.11
91404-01-01-02	53433	10173	2.89±0.49	1.27±0.11	54.091	0.09±0.01	1.51±0.02	4769.23±78.11	1.23
91404-01-01-03	53434	2547	4.52±0.58	1.21±0.10	75.706	0.12±0.01	1.53±0.02	5454.11±118.94	1.02
91404-01-01-01	53435	2067	2.11±0.45	1.72±0.08	265.00	0.09±0.01	1.24±0.06	6839.8	1.45
91702-01-01-00	53436	5185	1.06±0.46	1.60±0.07	288.04	1.14±0.48	1.24±0.03	9026	0.86
91404-01-01-04	53436	1377	3.39±0.56	1.28±0.09	136.46	0.14±0.02	1.54±0.02	7783.94±166.04	1.06
91702-01-01-01	53437	1860	3.31±0.54	1.19±0.10	131.19	1.75±1.25	1.59±0.01	9524.05±136.54	1.77
91704-04-01-00	53439	3476	0.67±0.32	1.73±0.04	792.38	1.55±0.51	1.29±0.03	8454.2	1.28
91702-01-02-03	53441	2059	*	1.15±0.01	7840.8	14.95±1.98	2.00±0.02	7304.1	1.48
91702-01-03-00	53443	13805	1.91±0.17	1.13±0.01	15095	21.83±3.42	1.99±0.01	7623.11±41.41	1.57
91702-01-05-00	53445	11923	2.22±0.15	1.19±0.01	20883	22.03±3.48	2.09±0.01	7637.38±38.07	1.14
91702-01-07-00	53448	13580	4.15±0.25	1.19±0.01	22486	22.85±3.31	3.83±0.07	6480.6	1.79
							2.13±0.06		
91702-01-10-00	53452	10901	8.71±0.26	1.32±0.01	16588	14.43±2.51	5.06±0.03	15165.7±495.15	1.81
91702-01-13-00	53454	15047	6.23±0.31	1.16±0.01	12056	1.71±0.02	3.60±0.04 (1)	9596.8	1.95
91702-01-13-00							2.39±0.04 (2)		

Table 6:

Obs. ID	Date (MJD)	Obs. Time (s)	#N_H atoms ($10^{22} cm^{-2}$)	Disk BB T_{in} (keV)	Disk BB[a] Flux ($10^-12 erg cm^{-2} s^{-1}$)	R_{in} (km)	Power-Law Photon Index	Power-Law[a] Flux ($10^{-12} erg cm^{-2} s^{-1}$)	χ^2_{red} (d.o.f.
91702-01-18-01	53460	4153	13.08±0.37	1.40±0.01	9980.4	9.63±1.99	5.75±0.06	14294±543.73	1.55 (8
91702-01-19-01	53464	3039	12.49±0.30	1.42±0.01	10610	9.55±2.02	5.64±0.06	14929.6±441.67	1.39 (8
91702-01-23-00	53465	18370	13.11±0.37	1.45±0.01	11172	0.89±0.01	5.67±0.03	16993.7±534.896	2.40 (8
91702-01-25-01	53467	3907	12.06±0.34	1.41±0.01	11874	10.31±2.05	5.61±0.05	15701.7±470.28	1.67 (8
91702-01-27-01	53470	2885	11.20±0.44	1.40±0.01	12783	10.80±2.34	5.40±0.05	16126.6±693.82	1.26 (8
91702-01-29-01	53471	2141	10.33±0.32	1.38±0.01	12979	11.34±2.38	5.28±0.04	15196.9±457.20	1.29 (8
91702-01-30-00	53472	7260	13.46±0.28	1.40±0.01	11048	10.06±1.79	5.95±0.05	16502.8±435.19	1.64 (8
91702-01-31-00	53474	10755	12.59±0.31	1.40±0.01	13334	11.13±1.86	5.75±0.03	19210.0±565.16	1.64 (8
91702-01-33-00	53476	7076	10.90±0.21	1.39±0.01	14890	11.95±2.24	5.43±0.03	18486.4±391.44	1.38 (8
91702-01-35-00	53479	5795	11.80±0.27	1.35±0.01	11573	11.35±2.30	5.81±0.05	14949.4±464.82	1.59 (8
91702-01-37-00	53482	10414	12.77±0.26	1.37±0.01	13826	11.87±2.05	5.89±0.04	19569.5±493.79	1.81 (8
91702-01-40-00	53486	3447	11.80±0.30	1.37±0.01	14963	12.45±2.26	5.83±0.05	19197.6±510.77	1.45 (7
91702-01-41-00	53487	2133	10.59±0.25	1.35±0.01	15828	13.30±2.81	5.57±0.05	17714.9±427.92	1.81 (8
91702-01-41-02	53487	2490	9.85±0.29	1.35±0.01	16881	13.82±3.03	5.38±0.05	17423.8±668.54	1.40 (8
91702-01-44-03	53490	1587	17.53±0.19	1.39±0.01	11604	10.60±2.22	6.13±0.04	36562.6±433.11	1.64 (8
91702-01-47-00	53493	10470	17.66±0.18	1.44±0.01	12857	10.16±1.69	6.18±0.28	37632.8±443.56	1.92 (8

Table 7:

Obs. ID	Date (MJD)	Obs. Time (s)	#N_H atoms ($10^{22} cm^{-2}$)	Disk BB T_{in} (keV)	Disk BB[a] Flux ($10^-12 erg cm^{-2} s^{-1}$)	R_{in} (10 kpc)	Power-Law Photon Index	Power-Law[a] Flux ($10^{-12} erg cm^{-2} s^{-1}$)	χ (d.
91702-01-49-00	53496	13988	14.55±0.27	1.35±0.01	12759	11.89±2.57	5.56±0.02 (1)	32804	2.11
							1.01±0.38 (2)		
91702-01-52-02	53500	2731	1.20±0.16	1.37±0.01	26783	16.61±2.50	2.35±0.01	15815.2±68.14	1.18
91702-01-54-00	53502	3633	2.48±0.18	1.39±0.01	15623	12.18±3.26	2.78±0.01	45326.0±223.50	1.12
91702-01-55-02	53504	1560	1.53±0.17	1.35±0.01	24053	16.39±2.59	2.36±0.02	14298.0±74.81	1.38
91702-01-58-03	53506	1061	2.01±0.19	1.49±0.02	23685	12.39±3.24	2.75±0.01	58237.2±255.25	1.30
91702-01-58-02	53507	2021	1.50±0.31	1.42±0.01	20769	13.23±3.73	2.72±0.01	42440.9±195.97	1.44
91702-01-58-00	53508	7534	5.89±0.08	4.71±0.08	8298.4	0.50±0.05	2.90±0.01	125998±195.85	1.61
91702-01-59-02	53509	3997	3.09±0.16	1.46±0.02	12752	9.66±3.10	2.80±0.01	72162.8±207.26	1.68
91702-01-60-00	53510	10613	1.37±0.18	1.41±0.01	22187	13.95±3.07	2.65±0.01	31419.3±91.65	1.59
91702-01-61-01	53512	6370	2.09±0.19	1.29±0.01	26068	1.87±0.01	2.89±0.05 (1)	9288.7	1.48
91702-01-61-01							2.11±0.03 (2)		
91702-01-61-03	53513	3528	0.76±0.19	1.36±0.01	26329	16.82±3.03	2.22±0.02	9583.52±54.56	1.38
91702-01-62-01	53514	2943	0.75±0.17	1.35±0.01	27249	17.39±3.03	2.26±0.02	7766.94±48.98	1.30
91702-01-64-00	53516	7369	1.15±0.17	1.39±0.01	21532	14.42±2.99	2.54±0.01	36578.8±117.30	1.71
91702-01-67-00	53518	3508	1.03±0.16	1.31±0.01	24300	18.05±2.79	2.28±0.01	16142.1±56.64	1.07
91702-01-66-02	53521	7501	1.42±0.14	1.27±0.01	25253	20.00±2.51	2.08±0.01	7182.00±40.20	1.27
91702-01-70-00	53522	6969	1.66±0.15	1.23±0.01	22146	1.96±0.01	2.12±0.02	4767.55±36.25	1.36

Table 8:

Obs. ID	Date (MJD)	Obs. Time (s)	$\#N_H$ atoms $(10^{22}cm^{-2})$	Disk BB T_{in} (keV)	Disk BB[a] Flux $(10^{-}12ergcm^{-2}s^{-1})$	R_{in} (10 kpc)	Power-Law Photon Index	Power-Law[a] Flux $(10^{-12}ergcm^{-2}s^{-1})$	χ^2_{red} (d.o.f.
91702-01-72-02	53526	3471	1.60±0.17	1.22±0.01	21496	1.99±0.01	2.10±0.01	11105.8±67.51	1.63 (8
91702-01-73-01	53530	2321	0.61±0.19	1.20±0.01	10550	15.01±2.67	2.09±0.01	7289.96±55.97	1.25 (8
91702-01-78-04	53533	2694	1.49±0.20	1.15±0.01	14077	1.91±0.02	1.98±0.02	9779.04±89.60	1.34 (8
91702-01-78-02	53537	2604	0.47±0.17	1.13±0.01	12025	1.83±0.01	1.98±0.01	7485.52±85.24	1.05 (8
91702-01-83-01	53539	10244	0.99±0.18	1.08±0.01	10129	1.96±0.02	1.93±0.01	6146.36±49.12	1.71 (8
91702-01-84-01	53542	3291	1.03±0.21	1.00±0.01	7463.1	2.13±0.02	1.98±0.07	1343.10±53.36	1.08 (8
91702-01-89-00	53545	6822	1.62±0.18	0.97±0.01	6362.2	22.72±3.98	1.96±0.15	426.64±39.25	1.20 (8
91702-01-92-00	53549	7114	1.34±0.18	0.96±0.01	5767.9	22.46±3.97	1.89±0.13	467.96±44.26	1.04 (8
91702-01-93-00	53550	14075	1.40±0.19	0.96±0.01	5706.4	22.22±3.86	1.78±0.10	492.94±41.69	1.04 (8
91702-01-95-02	53553	6705	1.37±0.21	0.97±0.01	5810.3	21.72±4.22	2.59±0.23	306.89±16.19	1.10 (8
91702-01-98-00	53555	3642	1.49±0.21	0.96±0.01	6305.3	22.92±4.43	2.60±0.48	170.65±16.44	1.25 (8
91702-01-01-13	53557	7125	1.14±0.19	0.99±0.01	6646.2	21.76±4.04	2.45±0.19	340.53±8.39	1.14 (8
91702-01-05-10	53562	7329	1.58±0.17	1.00±0.01	8232.1	23.43±3.74	1.79±0.08	678.29±46.64	1.45 (8
91702-01-07-10	53564	11026	1.90±0.20	1.00±0.01	8818.2	24.09±4.24	2.35±0.15	377.27±9.09	1.49 (8
91702-01-08-11	53565	2879	1.73±0.18	1.01±0.01	8943.9	23.48±4.10	1.79±0.17	618.81±84.76	0.91 (8
91702-01-09-11	53567	7898	1.84±0.16	1.01±0.01	9359.7	23.72±3.77	1.86±0.11	512.23±43.10	1.35 (8
91702-01-11-10	53569	10133	1.84±0.17	1.02±0.01	9723.3	23.78±3.80	1.82±0.10	556.23±41.44	1.52 (8
91702-01-21-10	53580	5886	1.58±0.18	1.04±0.01	10715	23.25±3.81	1.91±0.06	1271.13±49.84	1.25 (8

Table 9:

Obs. ID	Date (MJD)	Obs. Time (s)	$\#N_H$ atoms ($10^{22} cm^{-2}$)	Disk BB T_{in} (keV)	Disk BB[a] Flux ($10^-12 erg cm^{-2} s^{-1}$)	R_{in} (10 kpc)	Power-Law Photon Index	Power-Law[a] Flux ($10^{-12} erg cm^{-2} s^{-1}$)	χ (d.
91702-01-29-10	53590	6813	1.70±0.16	1.01±0.01	9113.5	23.67±3.80	1.87±0.09	820.97±50.21	1.24
91702-01-35-10	53600	2957	*	1.06±0.01	7042.8	17.66±2.42	1.95±0.02	6063.60±75.61	1.09
91702-01-39-11	53604	6443	*	1.04±0.01	5937.4	17.56±2.08	1.83±0.02	4205.71±58.28	1.28
91702-01-47-10	53610	4009	*	0.92±0.01	3419.4	19.50±2.50	1.97±0.07	611.55±35.79	0.89
91702-01-74-02	53625	2079	*	0.77±0.01	1001.2	19.30±4.50	2.21±0.03	1574.86±35.89	1.51
91702-01-75-00	53626	7471	*	0.70±0.01	630.56	2.16±0.03	3.14±0.05 (1)	2106.8	1.19
91702-01-75-00							1.65±0.04 (2)		
91702-01-76-02	53627	7069	*	0.59±0.01	356.04	3.07±0.10	3.00±0.03 (1)	2896.6	1.28
91702-01-76-02							3.87±0.21 (2)		
91702-01-79-01	53629	2974	*	1.38±0.02	581.50	0.23±0.01	1.94±0.02	522.28±66.95	1.92
91702-01-80-00	53631	10329	...	1.46±0.04	306.93	1.50±0.57	1.88±0.01	5091.61±47.43	1.37
91702-01-81-00	53633	3424	0.46±0.38	1.71±0.07	262.58	0.09±0.01	1.34±0.07	5137.4	1.06
91702-01-81-02	53635	5392	0.91±0.44	1.70±0.09	125.39	0.06±0.01	1.34±0.07	3688.8	1.01
91704-01-01-01	53637	13838	2.81±0.38	1.36±0.06	57.80	0.08±0.01	1.51±0.02	2890.67±56.95	1.22
91702-01-86-01	53639	2639	0.74±0.59	1.97±0.13	82.25	0.03±0.01	1.25±0.06	1075.5	0.90
91702-01-87-02	53642	10312	2.23±0.76	1.40±0.16	32.49	0.05±0.01	1.41±0.11	1037.6	0.97
91702-01-88-02	53644	3403	*	2.03±0.11	44.47	0.02±0.01	1.28±0.08	1296.26±141.71	1.04
91702-01-88-01	53645	2507	2.51±1.38	1.43±0.26	19.38	0.04±0.01	1.52±0.13	641.03±1095.82	0.86
91702-01-20-11	53647	6705	2.82±0.58	*	*	*	1.80±0.03	487.77±17.56	0.69
91702-01-30-11	53649	4074	*	1.90±0.19	16.40	0.02±0.01	1.40±0.24	347.29±106.53	0.84

Table 10: